1 **Supporting Information**

2

3 **Rubidium Fluoride Assisted High-efficiency Cu$_2$(Zn,Cd)SnS$_4$ Solar Cells by**

4 **Co-evaporation/annealing Method**

5  Shijin Wang[a,b], Lan Huang[b], Zi Ye[b], Lan Zhong[b], Guilin Chen[c,*], Jianmin Li [a,*], and Xudong Xiao [a,b,*]

6  a: School of Physics and Technology, Wuhan University, Wuhan 430072, China.

7  b: Department of Physics, The Chinese University of Hong Kong, Shatin 999077, Hong Kong.

8  c: College of Physics and Energy, Fujian Normal University, Fuzhou 350007, China.

9  E-mail: ljmphy@whu.edu.cn, glchen@fjnu.edu.cn, xdxiao@phy.cuhk.edu.hk, xdxiao@whu.edu.cn.

10  Corresponding authors: Jianmin Li (Dr. Li), Guilin Chen (Prof. Chen), Xudong Xiao (Prof. Xiao)

12 **Literature reviews**

13 **Table S1** Parameters of Rb-doped kesterite solar cells.

| Alkali | Absorber | Comparison | $PCE$ (%) | $V_{OC}$ (V) | $FF$ (%) | $J_{SC}$ (mA/cm$^2$) | Ref |
|---|---|---|---|---|---|---|---|
| RbF: Rb doped absorber target | CZTSSe | undoped | 6.25 | 300.4 | 62.6 | 33.2 | 1 |
| | | doped | 8.41 | 317 | 70.2 | 37.8 | |
| RbCl: Solution-based | CZTSSe | undoped | 4 | N/A | N/A | N/A | 2 |
| | | doped | 6.35 | 360 | 49.9 | 35.2 | |
| RbOH•$x$H$_2$O: Solution-based | CZTSSe | undoped | 4.13 | 407 | 41.32 | 24.56 | 3 |
| | | doped | 5.41 | 401 | 53.2 | 25.39 | |
| RbF: Solution-based | CZTSSe | undoped | 6.4 | 426.0 | 48.5 | 30.8 | 4 |
| | | doped | 5.7 | 441.1 | 44 | 29.6 | |

14 Interestingly, the impacts of Rb-doping are still unclear. In reference [1], [2], and [3], one can see an

15 improvement in efficiency after Rb-doping. Nevertheless, the change of performance parameters is not in the

16 same direction. For example, in reference [1], it is clear that $V_{OC}$, $J_{SC}$, and $FF$ all are improved after Rb

17 incorporation, while in reference [3], the $V_{OC}$ decreases. More impressively, the Rb-doping in reference [4]

18 shows a negative effect on device performance with an improved $V_{OC}$. All these works indicate that the role

19 of Rb in CZTSSe is complicated.

21 **Table S2** Efficiency evolution based on pure sulfide CZTS solar cells fabricated by thermal evaporation
22 method in recent ten years.

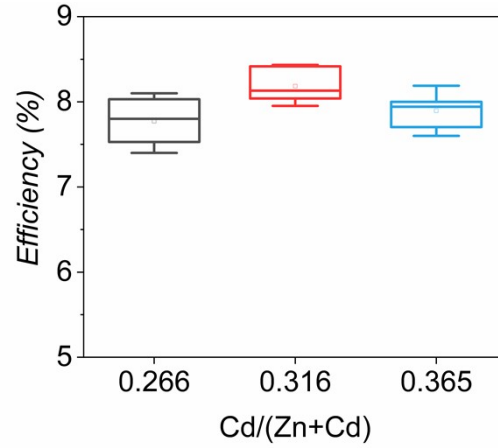| Years | Efficiency (%) | Ref |
|---|---|---|
| 2010 | 4.1 | [5] |
| 2010 | 6.81 | [6] |
| 2011 | 8.4 | [7] |
| 2014 | 2.56 | [8] |
| 2015 | 2.72 | [9] |
| 2015 | 4.61 | [10] |
| 2016 | 5.23 | [11] |
| 2017 | 2.25 | [12] |
| 2018 | 8.98 | [13] |
| 2019 | 5.6 | [14] |
| 2020 | 7.28 | [15] |
| 2020 | 8.31 | [16] |
| 2021 | 0.61 | [17] |

23 **Sn concentration optimization**
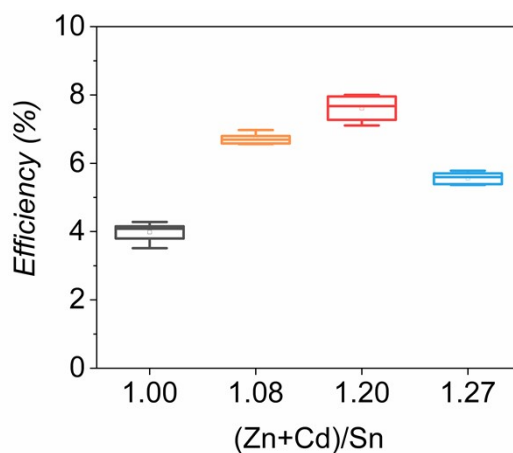


24

25 **Figure S1** Device efficiency statistics for CCZTS solar cells with different Sn concentrations.
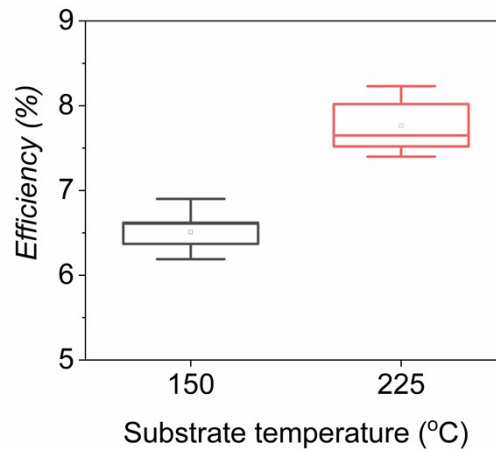
27 **Cd concentration optimization**



28

29 **Figure S2** Device efficiency statistics for CCZTS solar cells with different Cd concentrations.

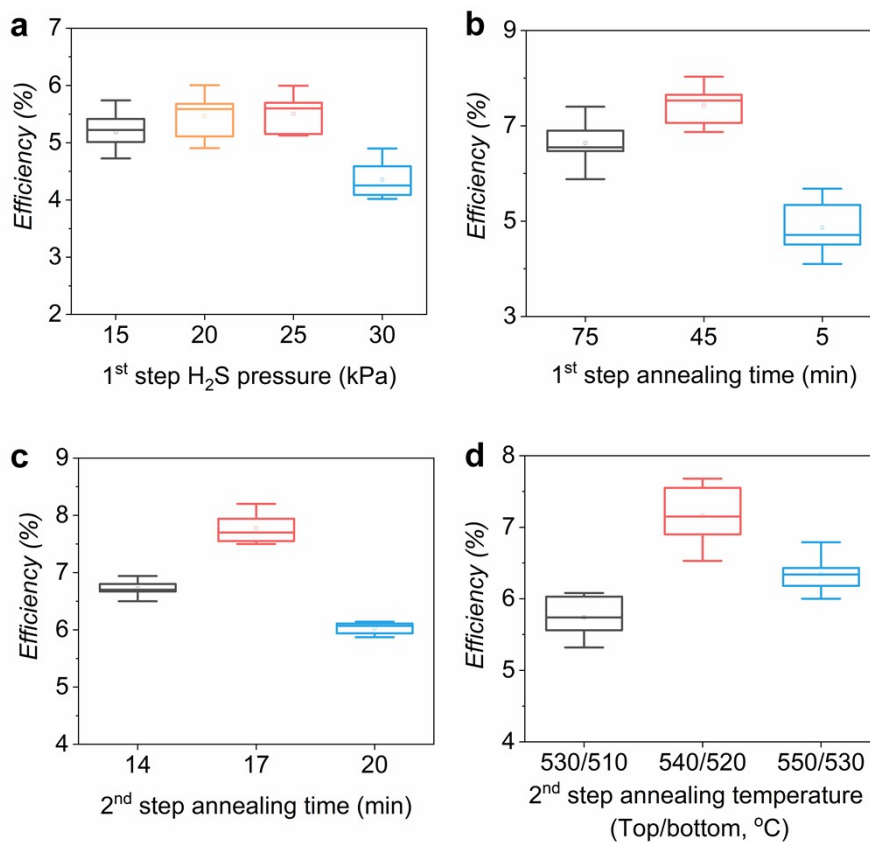30 **The substrate temperature optimization for precursor**



31

32 **Figure S3** Device efficiency statistics for CCZTS solar cells with precursors deposited under different

33 substrate temperatures.

**Post-annealing treatment process optimization**



**Figure S4** Device efficiency statistics for CCZTS solar cells related to (a) 1st step H$_2$S pressure, (b) 1st step annealing time, (c) 2nd step annealing time, and (d) 2nd step annealing temperature.

**Composition information of films**

**Table S3** Composition information of the absorbers under different Rb source temperatures.

| RbF source temperature | Cd/(Cd+Zn) | (Cd+Zn)/Sn | Cu/(Cd+Zn+Sn) | Rb/(Rb+Cu) | Denotation |
|---|---|---|---|---|---|
| control | 0.32 | 1.17 | 0.74 | 0 | control |
| 450°C | 0.33 | 1.21 | 0.74 | 0.53% | Rb-0.53% |
| 460°C | 0.33 | 1.21 | 0.73 | 0.87% | Rb-0.87% |
| 470°C | 0.33 | 1.19 | 0.73 | 1.19% | Rb-1.19% |
| 500°C | 0.33 | 1.18 | 0.75 | 2.16% | Rb-2.16% |

For all absorbers, the ratios of Cd/(Cd+Zn), (Cd+Zn)/Sn, and Cu/(Cd+Zn+Sn) are controlled within narrow ranges of 0.32-0.33, 1.17-1.21, and 0.73-0.75, respectively. As expected, with the increasing RbF source

44 temperature, the Rb/(Rb+Cu) ratio increases. In this work, the Rb/(Rb+Cu) ratio is controlled from 0 to 2.16%

45 after washing away the extra Rb on the crystalized CCZTS surface. For clear expression, the samples with

46 RbF cap layer under 450°C, 460°C, 470°C and 500°C are denoted as "Rb-0.53%", "Rb-0.87%", "Rb-1.19%",
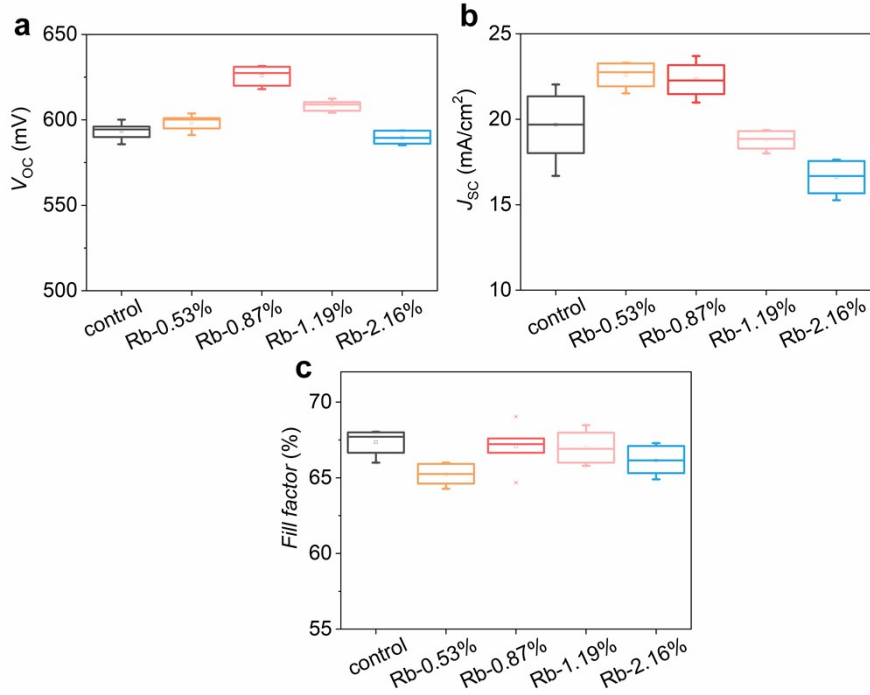
47 and "RbF-2.16%", respectively.

48

49 **SIMS measurement**
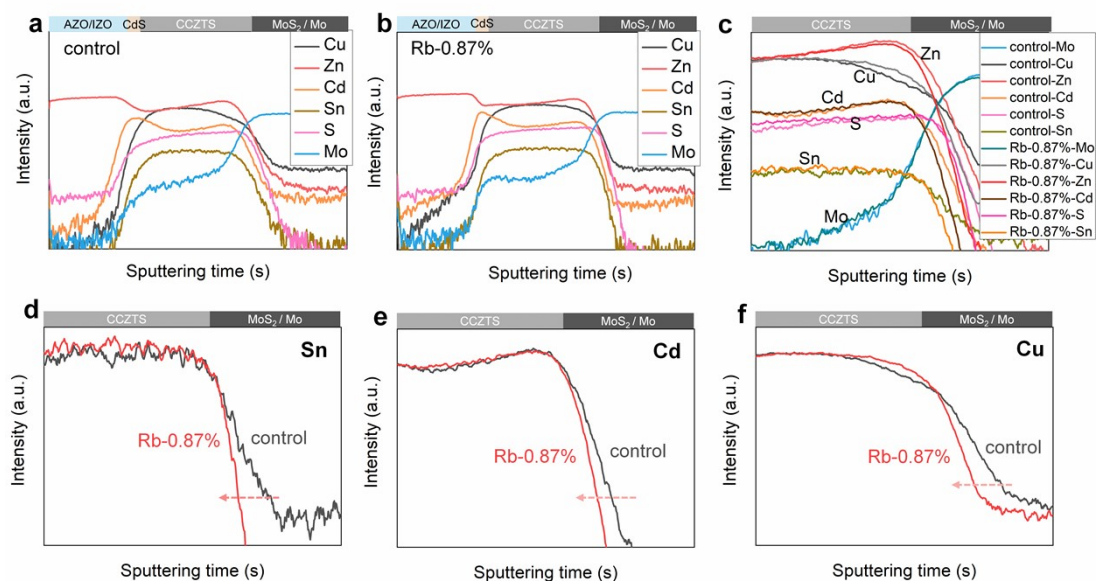


50

51 **Figure S5** Elemental distribution of Cu, Zn, Cd, Sn, S, and Mo in (a) "control" and (b) "Rb-0.87%". An

52 enlarged plot at the rear interface for both cells: (c) all elements, (d) Sn, (e) Cd, and (f) Cu.

54  **Performance boxplots**



55

56  **Figure S6** Statistic boxplots of $V_{OC}$, $J_{SC,}$ and *FF* for the CCZTS thin-film solar cells prepared with an RbF

57  layer deposited from a Knudsen cell with varied doping concentration.
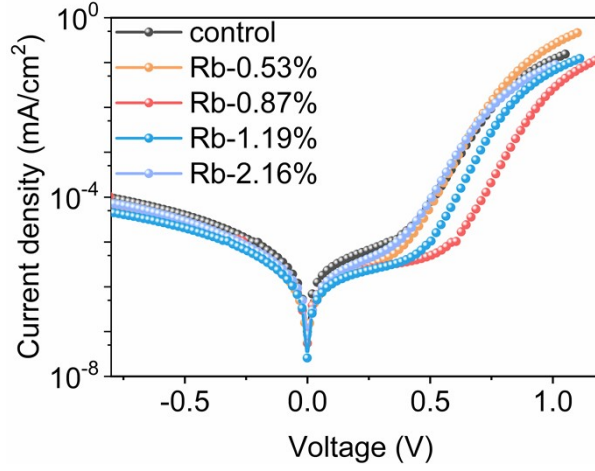

58  **Urbach energy calculation**

59  The value of Urbach energy ($E_U$) derived from EQE response could characterize the band tail states of the

60  CCZTS films, which provides an estimation of tail states by the following equation: [16, 18]

61  $\ln(EQE) = c + h\nu/E_U$                                      (1)

62  where *c* is a constant and hν is the bandgap energy.

64 **Dark *J-V* measurement**



65

66 **Figure S7** Dark *J-V* curves for the CCZTS thin-film solar cells prepared with an RbF layer deposited from

67 a Knudsen cell with varied doping concentration.

68 The diode quality factor (*A*) and the reverse saturation current density ($J_0$) could be estimated by the following

69 equation:

70 $\ln J = \ln J_0 + \dfrac{qV}{A k_B T}$

71 (2)

72 where $q$, $k_B$, and T are the elemental charge, Boltzmann constant, and temperature, respectively. According

73 to it, $J_0$ can be derived by extending the fitting line in the graph to 0 V, and *A* can be calculated from the

74 slope of the curve. Quantitatively, the $V_{OC}$ gain between two devices can be calculated using the following

75 equations:

76 $V_{OC} = \dfrac{AkT}{q} \ln\left(1 + \dfrac{J_{SC}}{J_0}\right) \approx \dfrac{AkT}{q} \ln\left(\dfrac{J_{SC}}{J_0}\right)$

77 (3)

78 $\Delta V_{OC} = \dfrac{AkT}{q} \ln\left(\dfrac{J_{SC}^{Rb-0.87\%}}{J_0^{Rb-0.87\%}} \times \dfrac{J_0^{control}}{J_{SC}^{control}}\right)$ (4)

79

81 *C-V* **measurement**

82 From *C-V* measurement, the relation between junction width and the charge density can be extracted and the

83 built-in potential ($V_{bi}$) according to the following equations:

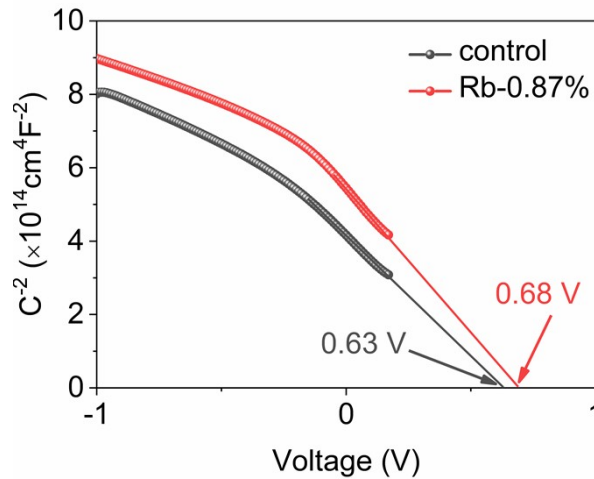84 $$N_{C-V} = \frac{C^3}{qS^2\varepsilon_0\varepsilon_r}(\frac{dC}{dV})^{-1}$$

85 (5)

86 $$W_d = \frac{S\varepsilon_0\varepsilon_r}{C}$$

87 (6)

88 $$\frac{1}{C^2} = \frac{2}{\varepsilon_0\varepsilon eS^2N}(V_{bi} - V)$$

89 (7)

90 Here, *C, S, V,* $\varepsilon_0$, $\varepsilon_r$, *N* and *q* are measured capacitance, effective area of the solar cell, positive/negative for

91 forward/reverse bias, and the vacuum permittivity, the relative dielectric constant of CCZTS film, the carrier

92 density, and elemental charge, respectively.

93



94 **Figure S8** $C^{-2}$-voltage curves for "control" and "Rb-0.87%".

**Band offset measurement and calculation**
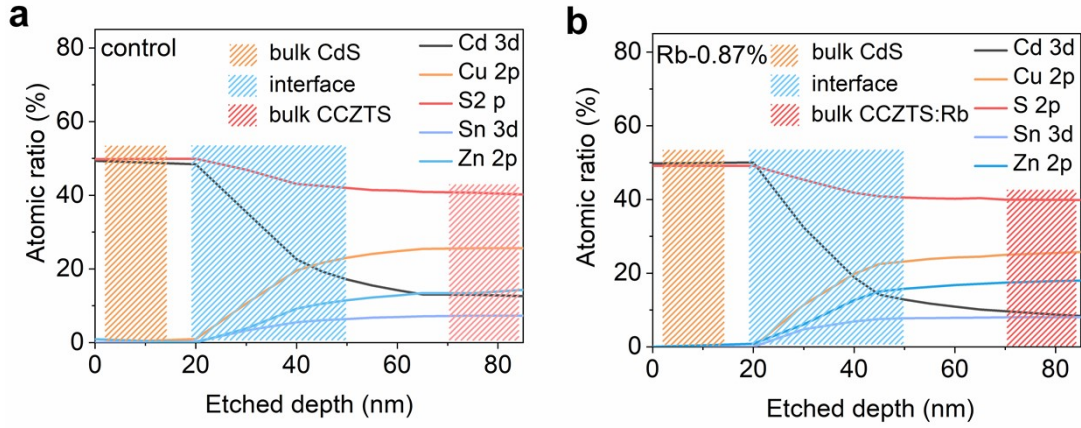


**Figure S9** XPS depth profile of Cu, Cd, Zn, Sn, and S at CdS/CCZTS:Rb interface starting from bulk CdS into bulk CCZTS:Rb. The etched depth is referred to $Ta_2O_5$ standard sample.

The elemental depth profiles of Cd, Cu, Zn, Sn, and S from CdS to CCZTS:Rb are detected by moderately sputtering with $Ar^+$ ions (1000 eV). According to the composition variation, three areas (bulk CdS area, interface area, and bulk CCZTS) area can be readily identified. With the known approach, the valence band offset (VBO) and the conduction band offset (CBO) of the CCZTS/CdS heterojunction can be calculated as shown below:[19, 20]

$$VBO = E_{VBM}^{CdS} - E_{VBM}^{CCZTS} + \Delta E \tag{8}$$

$$CBO = E_g^{CdS} - E_g^{CCZTS} - VBO \tag{9}$$

where $E_{VBM}^{CdS}$, $E_{VBM}^{CCZTS}$, $\Delta E$, $E_g^{CdS}$ and $E_g^{CCZTS}$ are the positions of valence band edges of bulk CdS and bulk CCZTS, band bending, the bandgap of CdS and CCZTS, respectively.
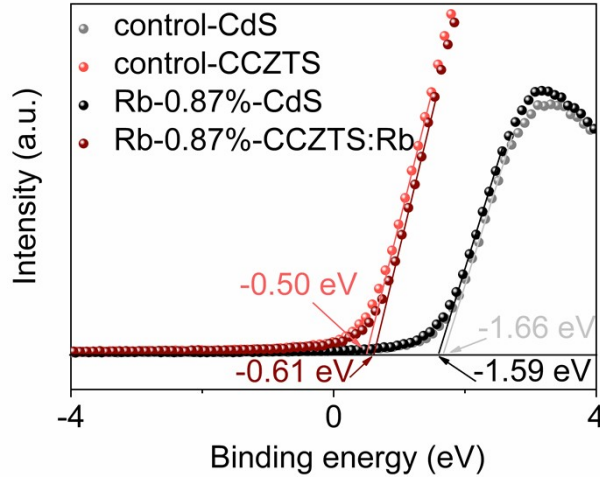
110
111 **Figure S10** The XPS valence band spectroscopy of the bulk CdS and bulk CCZTS or CCZTS:Rb for

112 "control" and " Rb-0.87%". The negative sign means the position is lower than the Fermi level.

113 It is clear to see that the $E_{VBM}$ (relative to Fermi level) of bulk CdS and bulk CCZTS:Rb are at -1.59 eV and

114 -0.61 eV, respectively, and that of bulk CdS and bulk CCZTS of "control" are at -1.66 eV and -0.50 eV,

115 respectively.
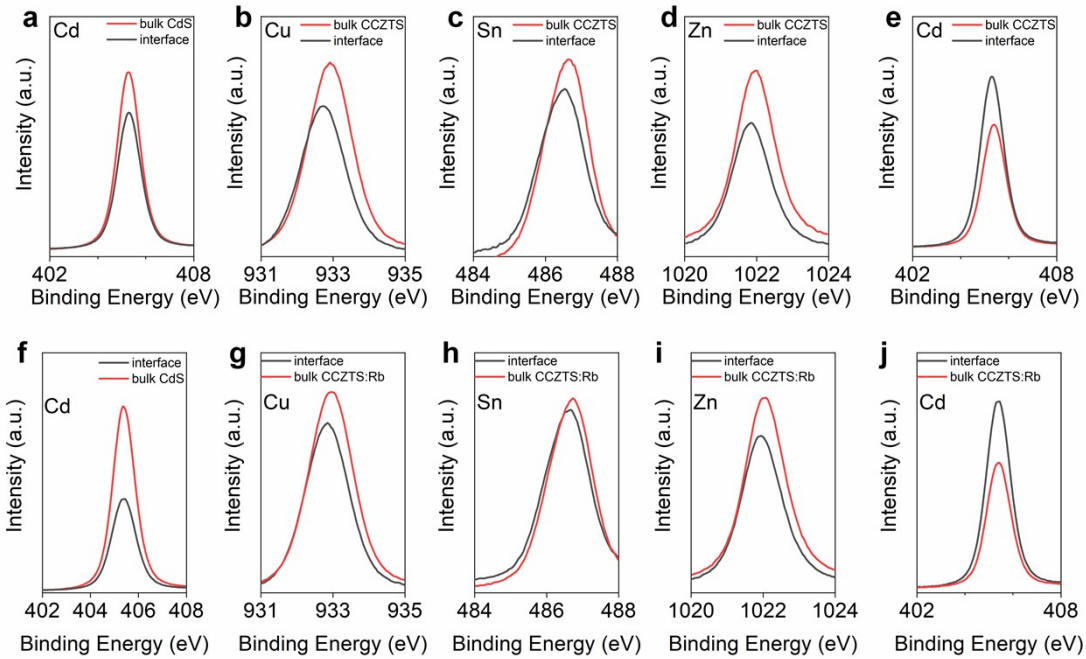


116
117 **Figure S11** The XPS peaks of the concerned element in the bulk and at the interface calibrated by C peak

118 (284.8 eV). (a-e) for "control", and (f-j) for " Rb-0.87%".

119 To calculate VBO, $\Delta E$ appears ultimately necessary, which can be easily derived by the well-known formula:

120 $$\Delta E_{CL} = \left(\Delta E_{CL}^{a} - \Delta E_{CL}^{a}(i)\right) + \left(\Delta E_{CL}^{b}(i) - \Delta E_{CL}^{b}\right) \qquad (10)$$

121 $$\Delta E = \frac{(\Delta E_{Cd/Cu} + \Delta E_{Cd/Zn} + \Delta E_{Cd/Cd} + \Delta E_{Cd/Sn})}{4}$$

122 (11)

123 where $\Delta E_{CL}^{a}$ and $\Delta E_{CL}^{b}$ are the core level energies of two selected elements in the bulk absorber (CCZTS or

124 CCZTS:Rb) and in the bulk buffer (CdS), and $\Delta E_{CL}^{a}(i)$ and $\Delta E_{CL}^{b}(i)$ are the core level energies of the

125 corresponding element at the interface. In the present case, the Cd is chosen in CdS and Cu, Zn, Cd, and Sn

126 are selected in CCZTS or CCZTS:Rb. The XPS peaks of each element in the bulk and at the interface are

127 plotted in **Figure S5**. These figures provide the peaks shift values of (Cd/Cu), (Cd/Zn), (Cd/Cd) and (Cd/Sn)

128 as discussed in the article. The associated values are summarized in **Table S4**.

129

130 **Table S4** XPS peak positions of all elements at the interface or in the bulk CdS and CCZTS films of "control"

131 and "Rb-0.87%" after calibration by C peak (284.8 eV).

| Samples | location | Cd 3d | Cu 2p | Sn 3d | Zn 2p |
|---------|----------|-------|-------|-------|-------|
| "Rb-0.87%" | CdS | 405.38 | | | |
| | interface | 405.38 | 932.83 | 486.58 | 1021.94 |
| | CCZTS:Rb | 405.39 | 932.94 | 486.68 | 1022.03 |
| control | CdS | 405.28 | | | |
| | interface | 405.29 | 932.71 | 486.47 | 1021.83 |
| | CCZTS | 405.38 | 932.91 | 486.61 | 1021.95 |

132 These data are extracted from **Figure S11** and used for calculating the band bending value. The values for

133 (Cd/Cu), (Cd/Zn), (Cd/Cd) and (Cd/Sn) in CCZTS:Rb are estimated to be 0.11 eV, 0.09 eV, 0.01 eV, and 0.1

134 eV, correspondingly, resulting in an overall average band bending value of 0.08 eV by using Equation (11).

135 With the same method, the bending for "control" is estimated to be 0.15 eV. The decreased $\Delta E$ by Rb-doping

136 should be attributed to the reduced defect states in bulk or at the interface of CCZTS film.

137
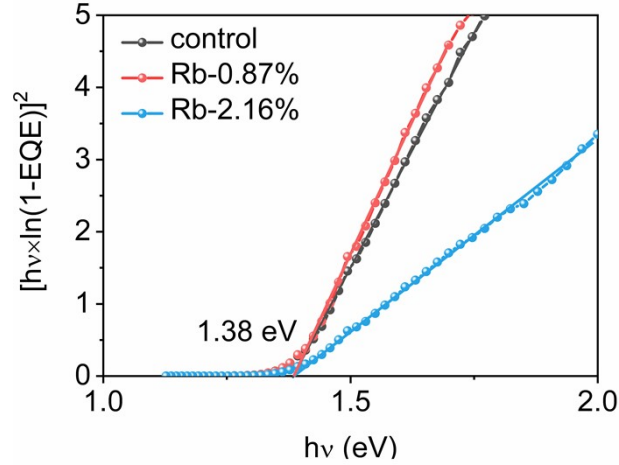
**Figure S12** Plot of $[h\nu \times \ln(1-EQE)]^2$ versus $h\nu$ of "control", "Rb-0.87%", and "Rb-2.16%".

This plot gives information on the bandgap value of the absorber. The three absorbers share the same bandgap with 1.38 eV, suggesting the Rb-doping in this work does not affect the bandgap. This may be explained by the low Rb-doping concentration.



142
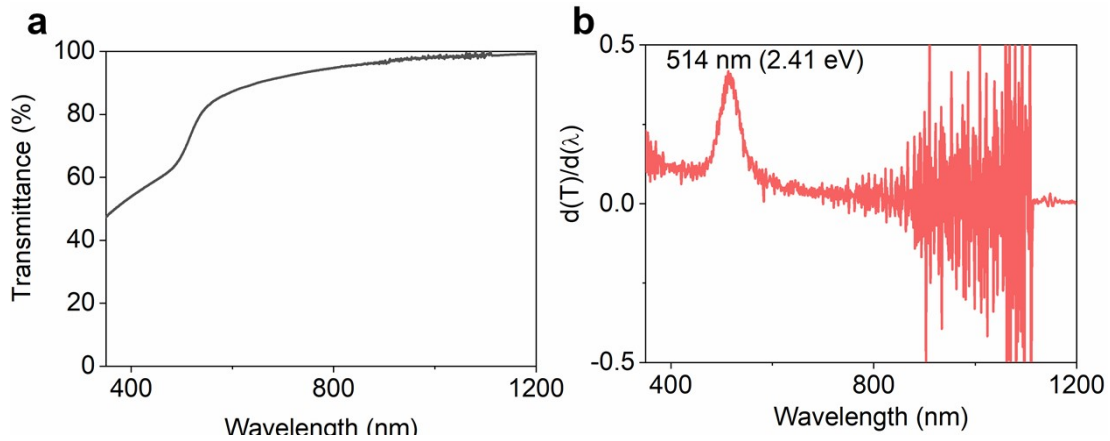
**Figure S13** (a) Transmittance spectra of CdS thin film directly deposited onto glass. (b) The plots of the differential of the transmittance to wavelength versus wavelength.

The differential curve in (b) exhibits a peak located at 514 nm, suggesting there is a strong absorption peak of CdS. Thus, the bandgap of CdS can be calculated to be 2.41 eV.

By combining the valence band edges of buffer and absorber, and the overall average band bending, the valence band offset (VBO) at CCZTS/CdS and CCZTS:Rb/CdS interface can be calculated to be -1.01 eV and -0.90 eV based on Equation (8). Therefore, the conduction band offset (CBO) can be derived to be 0.02 eV for CCZTS and 0.13 eV for CCZTS:Rb by Equation (9). Here, the bandgap of 1.38 eV for CCZTS film and of 2.41 eV for CdS are used.
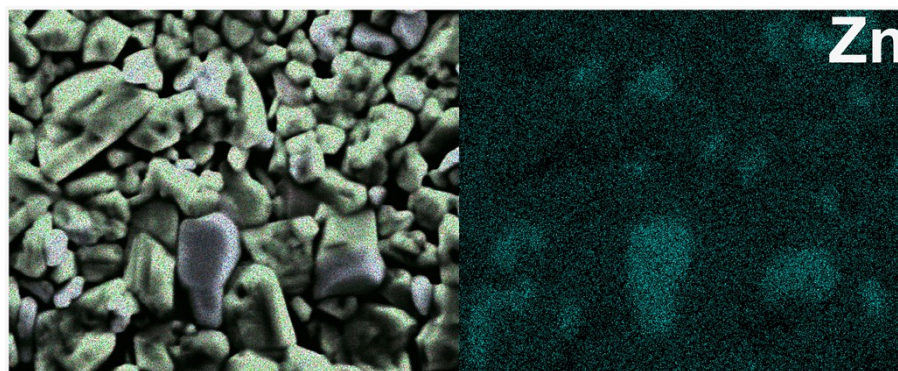
153 **SEM images**
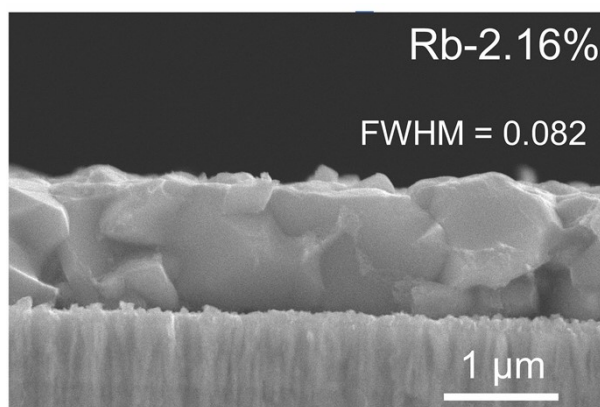


154

155 **Figure S14** Cross-view SEM image of "Rb-2.16%".

156 The FWHM of absorber of "Rb-2.16%" is 0.82, lower than those of "control" and "Rb-0.87%", suggesting

157 the bulk crystalnity is improved under higher Rb-doping concentration.

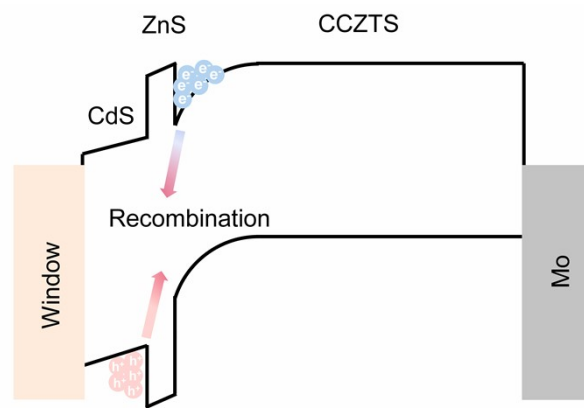158 **EDX mapping**



159

160 **Figure S15** (a) Top surface morphology and (b) EDX mapping of Zn element for "Rb-2.16%".

161 One can notice that there are lots of Zn-related particles on the top surface of the absorber.

164 **Figure S16** Schematic diagram of the role of ZnS particles at the interface of CCZTS/CdS.

165 This schematic is used for analyzing the mechanism of the ZnS-induced interface recombination. It is well-

166 known that the ZnS is a high resistive semiconductor with higher CBM and lower VBM than those of CCZTS

167 and CdS. Thus, the ZnS at the interface will act as a barrier for electrons and hole transport. As described,

168 the electrons and holes will accumulate at the interface, leading to a high recombination.

## References

1.      Wu, Y.; Zhao, M.; Zhuang, D.; Zhang, N.; Yu, X.; Wei, Y.; Lyu, X.; Ren, G.; Wang, C.; Hu, L., The effect of Rb doping on CZTSSe solar cells. *Solar Energy* **2019,** *187*, 269-273.

2.      Altamura, G.; Wang, M.; Choy, K.-L., Influence of alkali metals (Na, Li, Rb) on the performance of electrostatic spray-assisted vapor deposited Cu 2 ZnSn (S, Se) 4 solar cells. *Scientific reports* **2016,** *6* (1), 1-9.

3.      Hsieh, Y. T.; Han, Q.; Jiang, C.; Song, T. B.; Chen, H.; Meng, L.; Zhou, H.; Yang, Y., Efficiency enhancement of Cu2ZnSn (S, Se) 4 solar cells via alkali metals doping. *Advanced Energy Materials* **2016,** *6* (7), 1502386.

4.      Garud, S.; Vermang, B.; Sahayaraj, S.; Ranjbar, S.; Brammertz, G.; Meuris, M.; Smets, A.; Poortmans, J., Alkali Assisted Reduction of Open-Circuit Voltage Deficit in CZTSe Solar Cells. *physica status solidi c* **2017,** *14* (10), 1700171.

5.      Schubert, B. A.; Marsen, B.; Cinque, S.; Unold, T.; Klenk, R.; Schorr, S.; Schock, H. W., Cu2ZnSnS4 thin film solar cells by fast coevaporation. *Progress in Photovoltaics: Research and Applications* **2011,** *19* (1), 93-96.

6.      Wang, K.; Gunawan, O.; Todorov, T.; Shin, B.; Chey, S.; Bojarczuk, N.; Mitzi, D.; Guha, S., Thermally evaporated Cu 2 ZnSnS 4 solar cells. *Applied Physics Letters* **2010,** *97* (14), 143508.

7.      Shin, B.; Gunawan, O.; Zhu, Y.; Bojarczuk, N. A.; Chey, S. J.; Guha, S., Thin film solar cell with 8.4% power conversion efficiency using an earth-abundant Cu2ZnSnS4 absorber. *Progress in Photovoltaics: Research and Applications* **2013,** *21* (1), 72-76.

8.      Cui, H.; Liu, X.; Song, N.; Li, N.; Liu, F.; Hao, X., Impact of rapid thermal annealing of Mo coated soda lime glass substrate on device performance of evaporated Cu2ZnSnS4 thin film solar cells. *Materials Letters* **2014,** *125*, 40-43.

9.      Zhang, L.; Karthikeyan, S.; Sibakoti, M. J.; Campbell, S. A. In *Cu2ZnSnS4 thin film growth optimization and post rapid thermal annealing of solar cells and its influence on device performance*, 2015 IEEE 42nd Photovoltaic Specialist Conference (PVSC), IEEE: 2015; pp 1-6.

10.      Mise, T.; Tajima, S.; Fukano, T.; Higuchi, K.; Katagiri, H., Influence of chemical composition on the properties of directly coevaporated Cu–Zn–Sn–S-based thin films and solar cells. *Japanese Journal of Applied Physics* **2015,** *55* (1), 012303.

11.      Mise, T.; Tajima, S.; Fukano, T.; Higuchi, K.; Washio, T.; Jimbo, K.; Katagiri, H., Improving the photovoltaic performance of co-evaporated Cu2ZnSnS4 thin-film solar cells by incorporation of sodium from NaF layers. *Progress in Photovoltaics: Research and Applications* **2016,** *24* (7), 1009-1015.

12.      Shimamune, Y.; Jimbo, K.; Nishida, G.; Murayama, M.; Takeuchi, A.; Katagiri, H., Cu2ZnSnS4 formation by co-evaporation and subsequent annealing in S-flux using molecular beam epitaxy system. *Thin Solid Films* **2017,** *638*, 312-317.

13.      Liu, L.; Lau, T. K.; Zhi, Z.; Huang, L.; Wang, S.; Xiao, X., Modification of Mo back contact with MoO3− x layer and its effect to enhance the performance of Cu2ZnSnS4 solar cells. *Solar RRL* **2018,** *2* (12), 1800243.

14.      Baskaran, V.; Sakthivel, S., Current-voltage characteristics of Cu2ZnSnS4 absorber layer for energy harvesting devices. *Materials Research Express* **2020,** *6* (12), 126333.

15.      Huang, L.; Li, J.; Wang, S.; Zhong, L.; Xiao, X., Forming an ultrathin SnS Layer on Cu2ZnSnS4 surface to achieve highly efficient solar cells with Zn (O, S) Buffer. *Solar RRL* **2020,** *4* (5), 2000010.

16.      Huang, L.; Wang, S.; Zhong, L.; Chen, L.; Xiao, X., Role of ZnS Particles in the Performance of Cu2ZnSnS4 Thin Film Solar Cells: A Comparative Study by Active Control of Zinc Deposition in Coevaporated Precursors. *Solar RRL* **2020,** *4* (11), 2000334.

17.      Peksu, E.; Karaagac, H., Characterization of Cu2ZnSnS4 thin films deposited by one-step thermal evaporation for a third generation solar cell. *Journal of Alloys and Compounds* **2021,** *862*, 158503.

18.      Guchhait, A.; Su, Z.; Tay, Y. F.; Shukla, S.; Li, W.; Leow, S. W.; Tan, J. M. R.; Lie, S.; Gunawan, O.; Wong, L. H., Enhancement of open-circuit voltage of solution-processed Cu2ZnSnS4 solar cells with 7.2% efficiency by incorporation of silver. *ACS Energy Letters* **2016,** *1* (6), 1256-1261.

19.      Santoni, A.; Biccari, F.; Malerba, C.; Valentini, M.; Chierchia, R.; Mittiga, A., Valence band offset at the CdS/Cu2ZnSnS4 interface probed by x-ray photoelectron spectroscopy. *Journal of Physics D: Applied Physics* **2013,** *46* (17), 175101.

20.      Klein, A.; Löher, T.; Tomm, Y.; Pettenkofer, C.; Jaegermann, W., Band lineup between CdS and ultra high vacuum-cleaved CuInS 2 single crystals. *Applied physics letters* **1997,** *70* (10), 1299-1301.